Title

A fully-coupled fluid-structure interaction simulation of cerebral aneurysms

Journal

Computational Mechanics: Solids, Fluids, Structures, Fluid-Structure Interactions, Biomechanics, Micromechanics, Multiscale Mechanics, Materials, Constitutive Modeling, Nonlinear Mechanics, Aerodynamics, 46(1)

ISSN

1432-0924

Authors

Bazilevs, Y.
Hsu, M.-C.
Zhang, Y.
et al.

Publication Date

2010-06-01

DOI

10.1007/s00466-009-0421-4

Peer reviewed

Comput Mech (2010) 46:3–16
DOI 10.1007/s00466-009-0421-4

ORIGINAL PAPER

A fully-coupled fluid-structure interaction simulation of cerebral aneurysms

Y. Bazilevs · M.-C. Hsu · Y. Zhang · W. Wang · X. Liang · T. Kvamsdal · R. Brekken · J. G. Isaksen

Received: 7 August 2009 / Accepted: 13 September 2009 / Published online: 31 October 2009

Abstract This paper presents a computational vascular fluid-structure interaction (FSI) methodology and its application to patient-specific aneurysm models of the middle cerebral artery bifurcation. A fully coupled fluid-structural simulation approach is reviewed, and main aspects of mesh generation in support of patient-specific vascular FSI analyses are presented. Quantities of hemodynamic interest such as wall shear stress and wall tension are studied to examine the relevance of FSI modeling as compared to the rigid arterial wall assumption. We demonstrate the importance of including the flexible wall modeling in vascular blood flow simulations by performing a comparison study that involves four patient-specific models of cerebral aneurysms varying in shape and size.

Y. Bazilevs (✉) · M.-C. Hsu
Department of Structural Engineering, University of California, San Diego, 9500 Gilman Drive, La Jolla, CA 92093, USA
e-mail: yuri@ucsd.edu

Y. Zhang · W. Wang · X. Liang
Department of Mechanical Engineering, Carnegie Mellon University, Pittsburgh, PA 15213, USA

T. Kvamsdal
Department of Applied Mathematics, SINTEF Information and Communication Technology, 7465 Trondheim, Norway

R. Brekken
Department of Medical Technology, SINTEF Health Research, 7465 Trondheim, Norway

J. G. Isaksen
Departments of Neurosurgery and Neurology, University Hospital of North Norway, 9038 Tromsø, Norway

J. G. Isaksen
Institute of Clinical Medicine, University of Tromsø, 9037 Tromsø, Norway

Keywords Cerebral aneurysms · Fluid-structure interaction · Arterial wall tissue modeling · Incompressible Navier–Stokes equations · Boundary layer meshing · Wall shear stress · Wall tension

1 Introduction

In recent years patient-specific modeling of blood flow has matured immensely with the emergence of better imaging, modeling, mesh generation, computation and visualization technologies. State-of-the-art vascular modeling involves fully coupled fluid-structure simulations of large portions of the human cardiovascular system. Simulations are done in an effort to investigate hemodynamic factors influencing the onset and progression of cardiovascular disease, to predict an outcome of a surgical intervention, or to evaluate the effects of electromechanical assist devices.

The concept of patient-specificic vascular modeling was pioneered in [33]. A comprehensive set of computational procedures and complex-geometry patient-specific simulations were presented that went above and beyond the existing computational work on vascular blood flow. Over the next decade numerous improvements to the vascular blood flow simulation technology were proposed, such as the imposition of physiologically-realistic outflow boundary conditions [15,25,45], simulation of stenting technology in the context of cerebral aneurysms [1] and coronary arteries [49], optimization of cardiovascular geometries for surgical treatment [27], and inclusion of the effects of wall elasticity [4,5,14,36,42–44], and growth and remodeling [13] in the simulations.

In this article, we describe a collection of computational procedures that allow for high-fidelity simulation of vascular blood flow and flow-structure interaction of cerebral aneurysms. In Sect. 2, we give an overview of mesh genera-

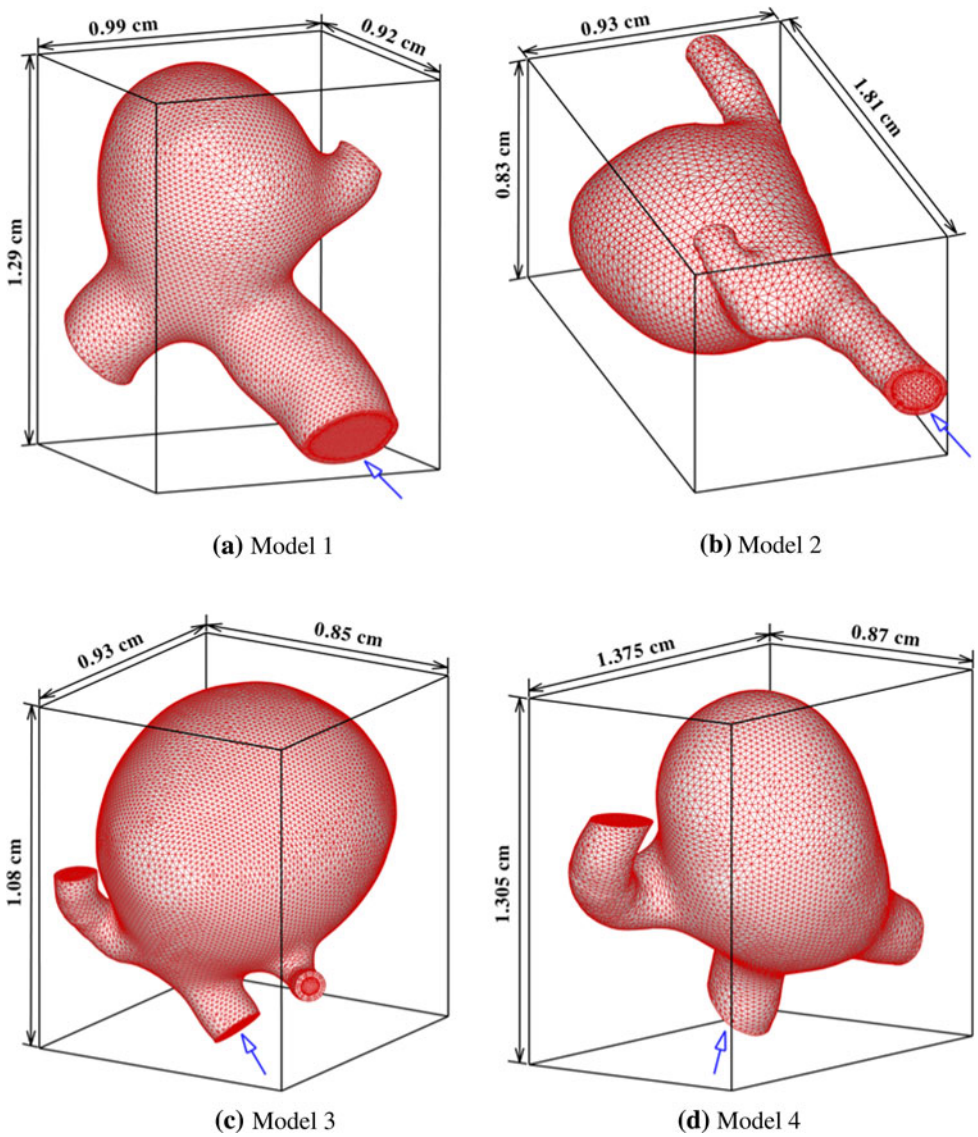

Fig. 1 Dimension, reference geometry and the constructed mesh for models 1–4

tion techniques from medical imaging data that are adapted to fluid-structure interaction (FSI) analysis. Our meshes contain both the fluid and solid elements for an appropriate discretization of the coupled problem, and boundary layer fluid elements near the arterial wall to better capture the boundary layer phenomena and accurately compute the wall shear stress. In Sect. 3, we review the coupled problem with the associated initial, boundary, and interface conditions, and give an overview of the computational procedures and details of extracting stresses from the computed solution fields. In Sect. 4, we present our simulation results, focusing on the comparison between the rigid and flexible wall simulations. While the differences in the computed blood flow speeds are not as significant (although clearly visible in some cases), the wall shear stress was found to be consistently overestimated in the rigid wall simulations, in one case by as much as 30%, which is quite significant. In Sect. 5, we draw conclusions and identify important future directions that would enhance the current state of cerebral aneurysm simulations.

2 Mesh generation for vascular fluid-structure interaction

We have developed a comprehensive and robust finite element meshing approach for patient-specific arterial geometries coming from medical imaging data, with emphasis on cerebral aneurysm configurations. The meshes contain both the blood volume and solid arterial wall, and are compatible at the fluid-solid interface. There are four main steps in our approach: (i) Image segmentation and geometric model construction; (ii) Tetrahedral mesh generation for the fluid volume using the octree-based method; (iii) Mesh quality

improvement, in which edge-contraction, pillowing, optimization, geometric flow smoothing, and mesh cutting are applied to the fluid mesh; and (iv) Mesh generation for the blood vessel wall. Below we give a brief summary of our meshing procedures. The reader is referred to [47] for further details on the methodology. The unique feature of our approach is that the meshes contain both the blood volume and solid arterial wall. This is in contrast to just the fluid meshes, which preclude the analyst from using three-dimensional solids to model the behavior of the arterial wall. The fluid-solid meshes are also compatible at their interface, which significantly simplifies analysis.

As a first step, the medical imaging data is loaded into CustusX [11], where the aneurysm is identified and segmented. A top-down octree-based subdivision and isocontouring method [46] is utilized to construct analysis-suitable tetrahedral meshes for just the fluid volume. For each octree cell we calculate a minimizer point using a quadratic error function, and then connect the minimizer points to construct tetrahedral elements. The above techniques may not produce sufficiently good quality meshes necessary for high-fidelity finite element simulations. Therefore, several post-processing techniques are adopted to improve the mesh quality. These include edge contraction, optimization, pillowing, smoothing, and mesh cutting. Edge contraction (i.e., removal of a mesh edge by collapsing its two endpoints) is used to remove the non-manifold situations.

Mesh quality improvement will be limited if all the four vertices of one tetrahedron lie on the model surface, or three vertices of one triangle are on the surface but the triangle is inside the volume. The pillowing technique can eliminate these two situations. In optimization-based geometric flow smoothing [48], the interior vertex is moved towards its center of mass, and each boundary vertex is restricted to move in its tangent plane.

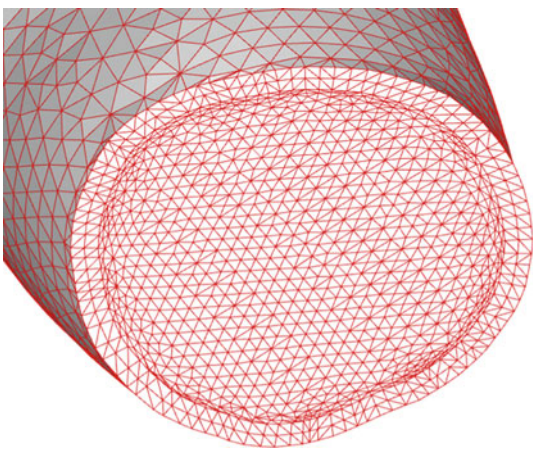

Fig. 2 Zoom on the mesh of the inlet surface of Model 1. Solid and boundary layer fluid mesh are shown

Table 1 Finite element mesh sizes for the aneurysm models

Model	Fluid elements	Solid elements	Total elements	Total nodes
1	271,889	82,236	354,125	64,033
2	94,957	41,940	136,897	25,123
3	646,943	72,262	719,205	125,879
4	258,540	79,890	338,430	60,938

Table 2 Inflow cross-sectional areas for the aneurysm models

Model	Inflow surface area (cm^2)
1	5.64×10^{-2}
2	2.44×10^{-2}
3	1.12×10^{-2}
4	4.17×10^{-2}

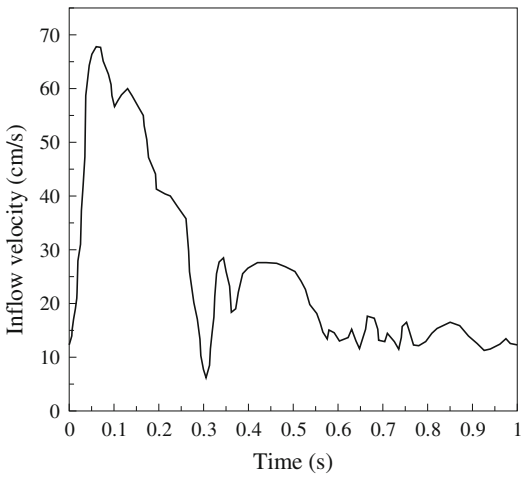

Fig. 3 Area-averaged inflow velocity as a function of time during the heart cycle

Mesh cutting is necessary to produce model inlets and outlets and allow imposition of physiologically realistic boundary conditions in FSI simulation. We use a single plane to cut each inlet or outlet branch to make sure all its vertices lie in the same plane. Mesh cutting typically impairs the mesh quality near the inlets and outlets, and necessitates further quality improvement.

As a last step, the blood vessel wall is constructed by extruding the surface mesh in an appropriately defined wall-normal direction by a prescribed amount.

The meshing techniques described here are general and apply to a large class of patient-specific vascular geometries. In this paper, we applied our meshing techniques to four patient-specific cerebral aneurysm models obtained from imaging data. These models, shown in Fig. 1, are employed in vascular FSI analysis presented later in the article.

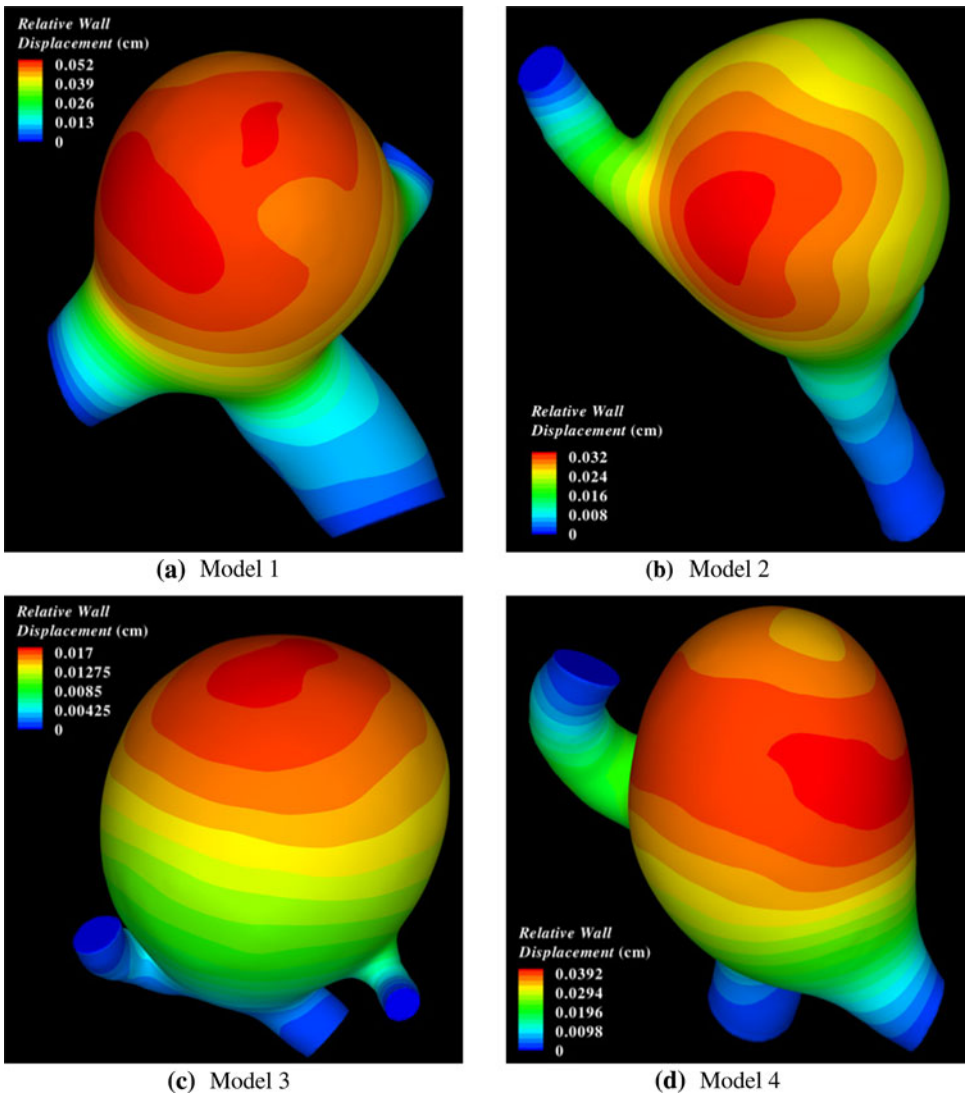

Fig. 4 Contours of wall displacement magnitude at $t = 0.08$ s, nearly peak systole. Wall displacement is taken relative to the configuration in low diastole

Remark We would also like to note that techniques with comparable functionality for extracting surface meshes from medical imaging and for mesh cutting were recently reported in [31].

3 Vascular fluid-structure interaction simulation

3.1 Continuum modeling

The arterial wall is modeled as a full three-dimensional large-deformation isotropic hyperelastic solid in the material description. We use the second Piola–Kirchhoff stress, $\boldsymbol{S}$, and its conjugate, the Green–Lagrange strain, $\boldsymbol{E}$, in the principle of virtual work, which leads to the weak form of the balance of linear momentum in the solid. The second Piola–Kirchhoff stress is obtained as a derivative of a scalar elastic potential, ψ, with respect to the Green–Lagrange strain as

$$\boldsymbol{S} = \frac{\partial \psi(\boldsymbol{E})}{\partial \boldsymbol{E}}, \tag{1}$$

where

$$\boldsymbol{E} = \frac{1}{2}(\boldsymbol{F}^T \boldsymbol{F} - \boldsymbol{I}), \tag{2}$$

and $\boldsymbol{F}$ is the deformation gradient with respect to material coordinates. The exact form of ψ employed here is given in [4] and corresponds to a neo-Hookean model with additional penalty on the volumetric part of the deformation. The model makes use of two material constants that can be identified with the tissue bulk and shear moduli, which, in turn, may be related to the material Young's modulus and Poisson's ratio using classical formulas. The stress-strain

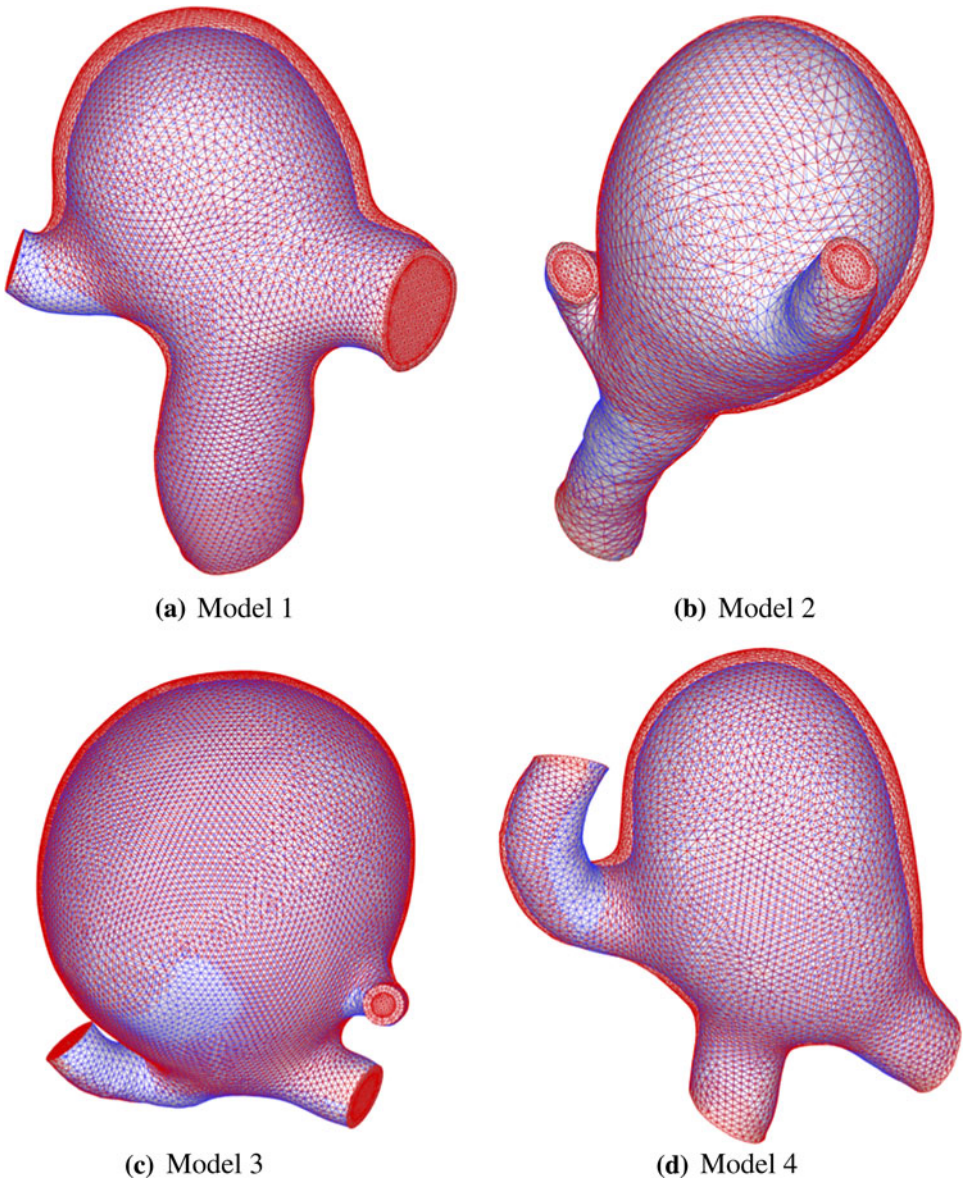

Fig. 5 Relative wall displacement between peak systole and low diastole

behavior of the material model was analytically studied on simple cases of uniaxial strain [4] and pure shear [26]. Stiffening with deformation was observed in both cases, which is a well-known characteristic of arterial tissue. In the computations presented in this paper, the density, Young's modulus, and Poisson's ratio of the arterial wall are set to $1.0\,\mathrm{g/cm^3}$, $10^7\,\mathrm{dyn/cm^2}$, and 0.45, respectively, as in [22]. The arterial wall thickness is taken to be approximately 0.018 cm. Given $\boldsymbol{S}$, the true or Cauchy stress, $\boldsymbol{\sigma}^s$, is obtained as (see, e.g. [17])

$$\boldsymbol{\sigma}^s = J^{-1}\boldsymbol{F}\boldsymbol{S}\boldsymbol{F}^T, \tag{3}$$

where $J = \det\boldsymbol{F}$ is the determinant of the deformation gradient.

We would like to note that in the computations presented in this article, the blood vessel configuration taken from image data is employed to approximate the reference, zero-stress configuration. However, in general, the vessel configuration coming from image data is not stress-free, which needs to be accounted for in the modeling. The reader is referred to [32,37] for a method of obtaining an estimated zero pressure geometry from patient-specific image data.

The blood flow is governed by the Navier–Stokes equations of incompressible flow posed on a moving domain. The Arbitrary Lagrangian–Eulerian (ALE) formulation is used, which is a popular approach for vascular blood flow applications [2,12,15,16]. Alternatively, one can apply the space-time methodology [36,40], which leads to better time accuracy. However, while a SSTFSI-SV technique proposed in [35] is quite comparable in cost to the ALE approach, in most cases the computational expense per time step is higher for space-time formulation.

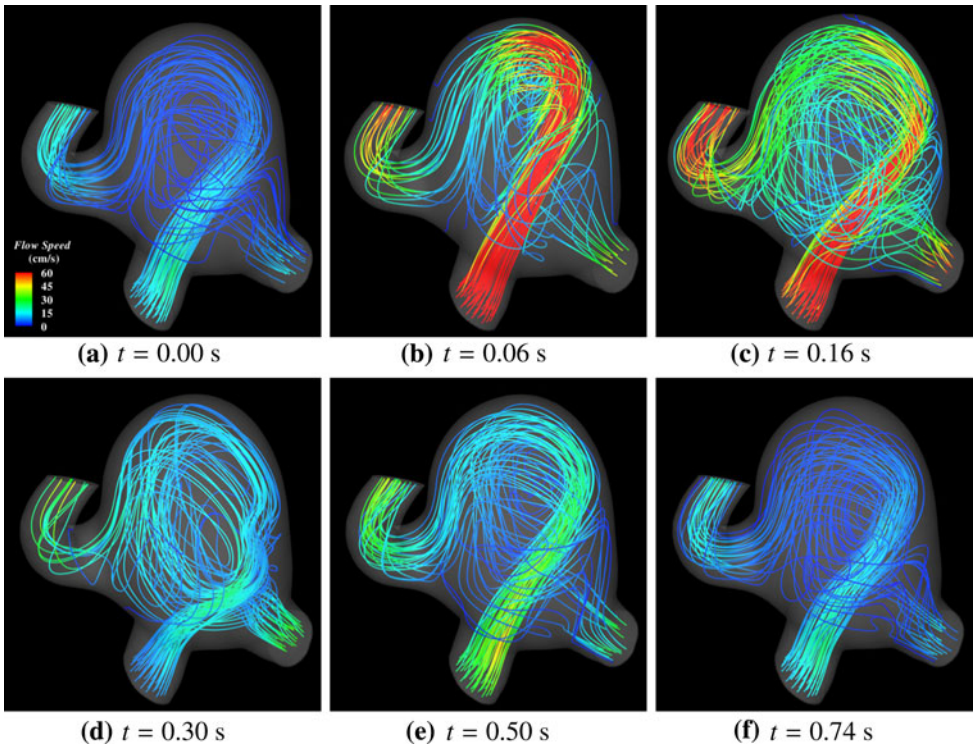

Fig. 6 Blood flow velocity streamlines of model 4 at various times during the heart cycle

The true or Cauchy stress for the incompressible Newtonian fluid is given through a constitutive law that holds on the spatial domain,

$$\boldsymbol{\sigma}^f = -p\boldsymbol{I} + 2\mu\boldsymbol{D}, \tag{4}$$

where p is the fluid pressure, μ is the dynamic viscosity, and $\boldsymbol{D}$ is the symmetric velocity gradient with respect to the spatial variables. In the computations the density and dynamic viscosity of the fluid are set to $1.0\,\mathrm{g/cm^3}$ and $0.04\,\mathrm{g/(cm\,s)}$, respectively.

No-slip boundary conditions hold at the fluid-solid interface. This means the fluid particles stick to the arterial wall. Furthermore, the following traction compatibility condition holds at the fluid-solid interface,

$$\boldsymbol{\sigma}^s\boldsymbol{n}^s + \boldsymbol{\sigma}^f\boldsymbol{n}^f = \boldsymbol{0}, \tag{5}$$

where $\boldsymbol{n}^s$ and $\boldsymbol{n}^f$ are the unit outward normal vectors to the fluid and solid subdomain boundary, respectively. This means that the fluid and solid forces are in equilibrium at the fluid-solid interface. Note that $\boldsymbol{n}^s = -\boldsymbol{n}^f$ in Eq. (5).

The fluid subdomain motion is governed by the equations of linear elasticity posed on a time-dependent "nearby" configuration, and are subject to the displacement boundary conditions coming from the motion of the arterial wall. This gives a well-defined current configuration of the fluid domain that conforms to the boundaries of the solid. In the discrete setting this procedure ensures a smooth evolution of the computation mesh of the fluid domain. The nearby configuration typically corresponds to that of the previous time step in our computations (see, e.g., [4]).

3.2 Discretization and solution strategies

The meshes for both fluid and solid regions consist of linear tetrahedral elements with a compatible discretization at the fluid-solid interface. The solid wall is meshed using two layers of tetrahedral elements in the through-thickness direction. Boundary layer meshing is employed in the fluid region to enhance the resolution of wall quantities, such as the shear stress. Boundary-layer mesh refinement was also used in [32] and [38]. The latter reference also included comparative results from meshes with and without boundary layer resolution. Figure 2 zooms on the inlet branch of Model 1 where one can clearly see the solid wall and the high-quality boundary layer fluid mesh. The meshes for the remaining three models are of similar quality. Mesh sizes for all models are summarized in Table 1. It is felt that very good mesh resolution is achieved in all cases.

The solid and fluid mesh motion equations are discretized using the Galerkin approach. The fluid formulation makes use of the recently proposed residual-based variational multiscale method [3]. The residual-based variational multiscale methodology is built on the theory of stabilized and multiscale methods (see [9] for an early reference, [21] for a comprehensive review, and [3,34] for specific expressions

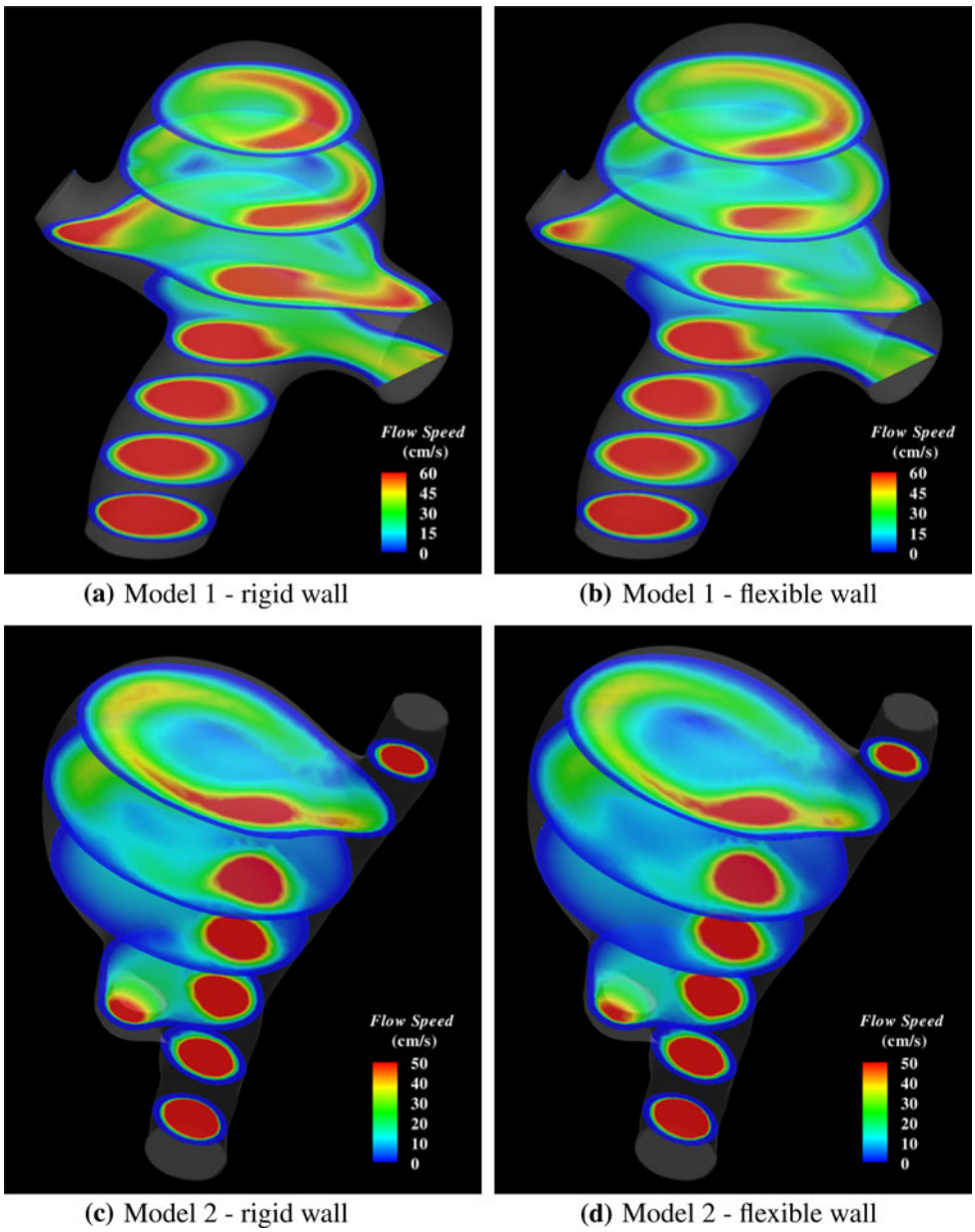

(a) Model 1 - rigid wall **(b)** Model 1 - flexible wall

(c) Model 2 - rigid wall **(d)** Model 2 - flexible wall

Fig. 7 Blood flow velocity magnitude on interior cuts. Data taken near peak systole ($t = 0.08\,\mathrm{s}$)

employed in the definition of stabilization parameters). The methodology applies equally well to laminar and turbulent flows and is thus attractive for applications where the nature of the flow solution is not known a priori. The time-dependent discrete equations are solved using the generalized-α time integrator proposed in [10] for the equations of structural mechanics, developed in [24] for fluid dynamics, and further extended in [4] to fluid-structure interaction. A monolithic solution strategy is adopted in which the increments of the fluid, solid, and mesh motion variables are obtained by means of a Newton–Raphson procedure in a simultaneous fashion (see [4,5] for details). The effect of the mesh motion on the fluid equations is omitted from the tangent matrix for efficiency, as advocated in [6].

3.3 Boundary conditions

Pulsatile velocity is applied at the inlet branch. We aim to simulate several cases whose inlet cross-sectional areas can vary significantly from one model to another (see Table 2). This variation is due to the use of patient-specific data, and is quite natural in practice. For the four models considered in this work, shown in Fig. 1, the ratio of the largest to smallest inlet cross-sectional area exceeds a factor of five. In this case, an attempt to impose the same volumetric flowrate as a function of time for all four models will result in the inflow velocity variation that is over a factor of five between the patients, which is not physiological. Instead, we chose to impose the same area-averaged inflow velocity for all models, which is

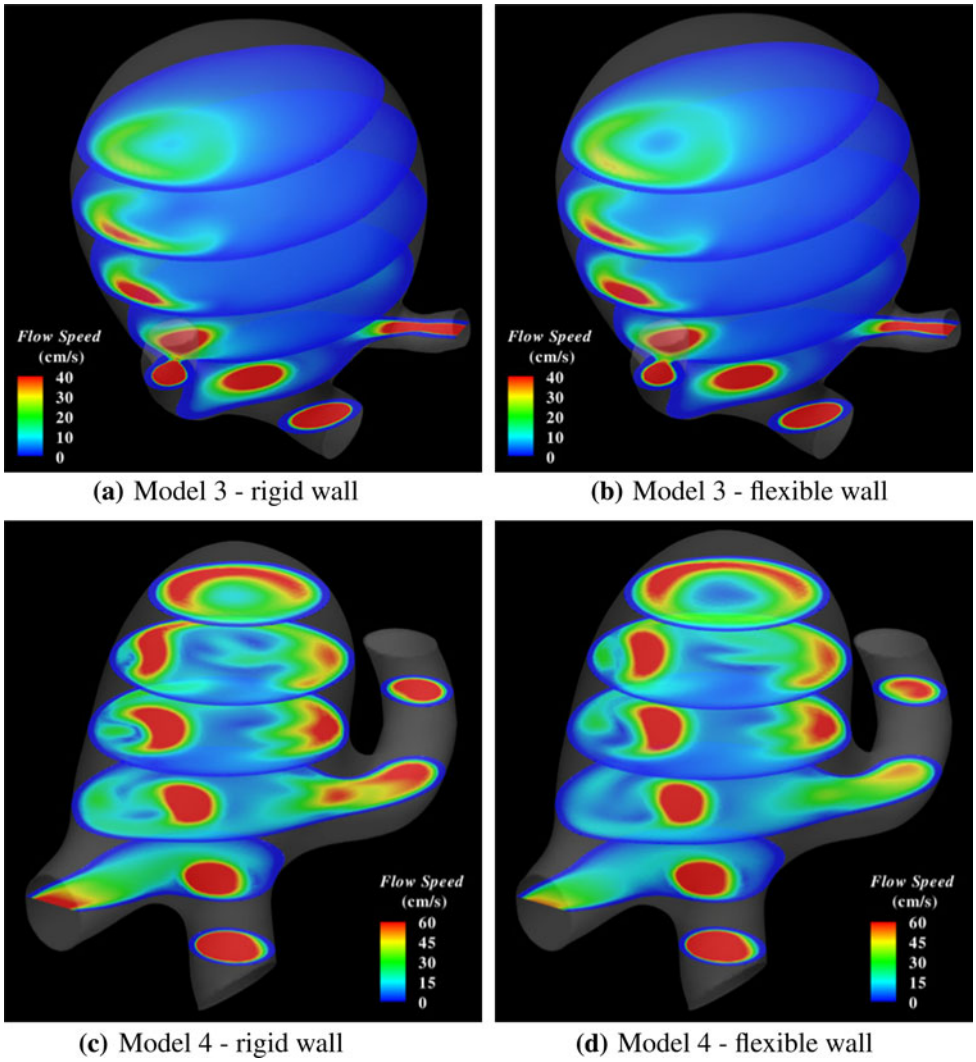

Fig. 8 Blood flow velocity magnitude on interior cuts. Data taken near peak systole ($t = 0.08\,\mathrm{s}$)

more realistic. Figure 3 shows the inlet velocity, adapted from [41], as a function of time during the heart cycle used as an inlet boundary condition for all models.

Remark A velocity profile mapping technique was described in [32], which (i) Maps a preferred velocity profile given over a circular cross-section to a non-circular cross-section; (ii) Provides a velocity profile that always integrates to a given flow-rate derived from the experimentally-observed velocity profile, which shares roots with what we see in Fig. 3.

Resistance boundary conditions are set at the outlet branches. They are posed such that physiological pressure levels are attained in the simulations (see [6,45] for more details). The solid wall is subjected to zero displacement at the inlet and outlet planes, and zero traction boundary condition at the outer surface. We would like to note that specifying only the zero normal component of the displacement at the model inlets and outlets, as done in [32,37], leads to more realistic global vessel wall displacement. However, the effect of this boundary condition on the wall shear stress and wall tension appears to be minor [39].

3.4 Extraction of derived quantities of hemodynamic interest from simulation data

While blood flow velocities and arterial wall displacements are directly defined at mesh nodes and are a simple matter to extract and visualize, extracting the wall shear stress (WSS) and the appropriately-defined wall tension (WT) quantities involves computational procedures that warrant explanation, which is what we do in this section.

The WSS at the fluid-solid interface, $\boldsymbol{\tau}$, is defined as a fluid traction vector restricted to the tangent plane of the interface surface, namely,

$$\boldsymbol{\tau} = \boldsymbol{\sigma}^f \mathbf{n}^f - (\mathbf{n}^f \cdot \boldsymbol{\sigma}^f \mathbf{n}^f)\mathbf{n}^f . \tag{6}$$

Note that, given the definition of $\boldsymbol{\sigma}^f$ in Eq. (4), the pressure does not contribute to the WSS. Also note that $\boldsymbol{\tau}$ can be

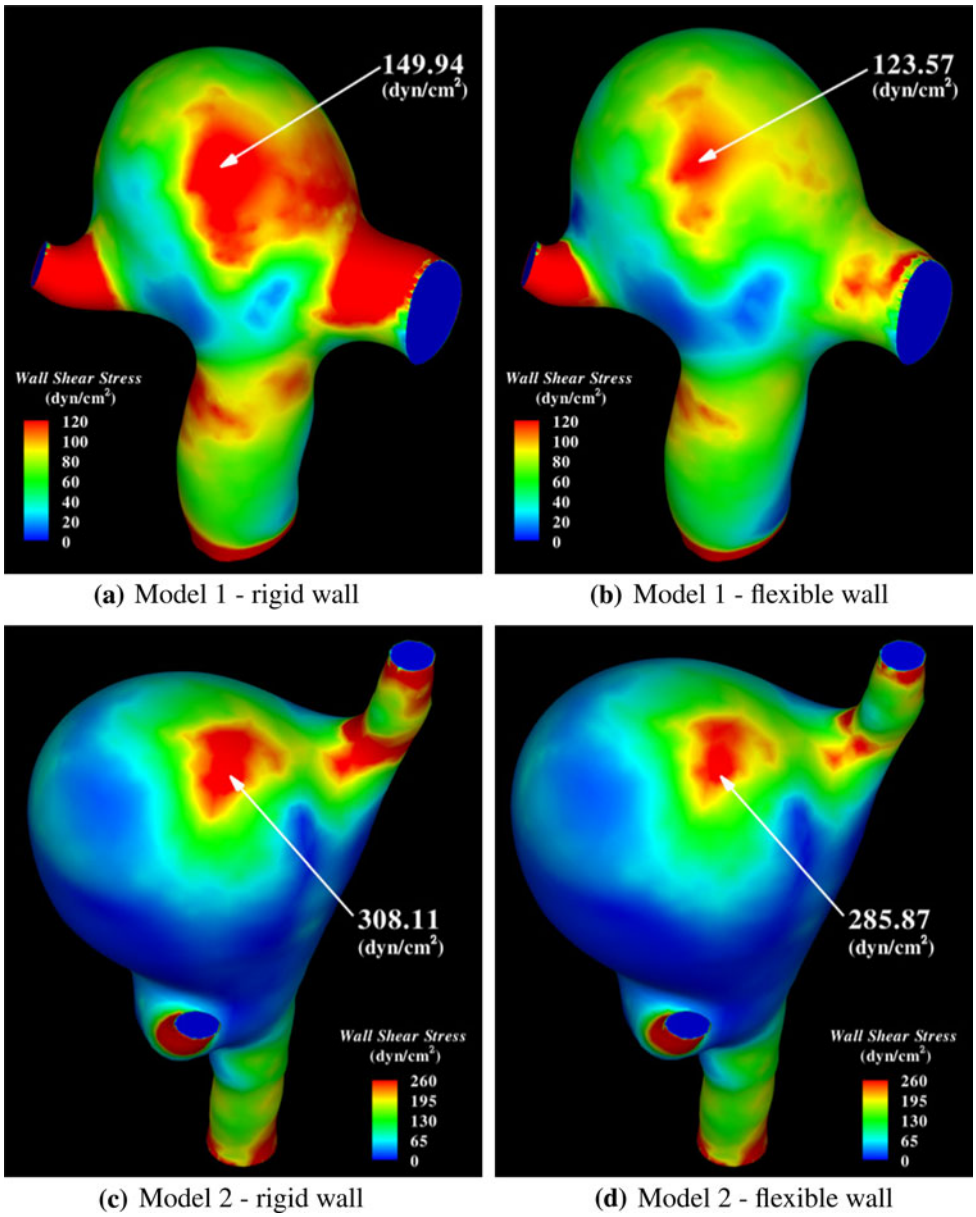

(a) Model 1 - rigid wall **(b)** Model 1 - flexible wall

(c) Model 2 - rigid wall **(d)** Model 2 - flexible wall

Fig. 9 Wall shear stress. Data taken near peak systole ($t = 0.08\,\mathrm{s}$)

computed using the definition of the Cauchy stress in the solid domain, owing to the compatibility condition (5). In the fully continuous setting both the fluid and solid definitions will produce identical results. On the other hand, in the discrete case, the answers will generally differ, although both quantities are expected to converge to the same value under mesh refinement. In this work, we adopt the definition that uses the fluid stress, which allows for a direct comparison with the rigid wall results.

The wall shear stress is computed as follows. We first perform an L_2-projection of the viscous stress tensor components onto the original finite element space of linear tetrahedral functions. This procedure, also employed in [23] for improved consistency of low-order stabilized finite element formulations of fluid flow phenomena, gives a convenient nodal-based definition of the viscous stress tensor. We then evaluate the traction vector using the reconstructed viscous stress tensor on the fluid-solid boundary, compute the WSS as in (6), and perform another L_2-projection onto the finite element space now spanned by the fluid-solid boundary basis functions. The latter reconstruction gives a convenient nodal definition of the WSS at the fluid-solid boundary that can be easily rendered using any finite element plotting software. The above procedure was suggested to us by Tezduyar and Takizawa [39] and used in computing the WSS reported in [32]. Other WSS postprocessing techniques, such as, for example, based on conservation ideas (see, e.g., [8,19,20,28]), may also be employed, but were not pursued here.

The wall tension is associated with aneurysm rupture and merits a close investigation (see, e.g., [22]). Aneurysm walls

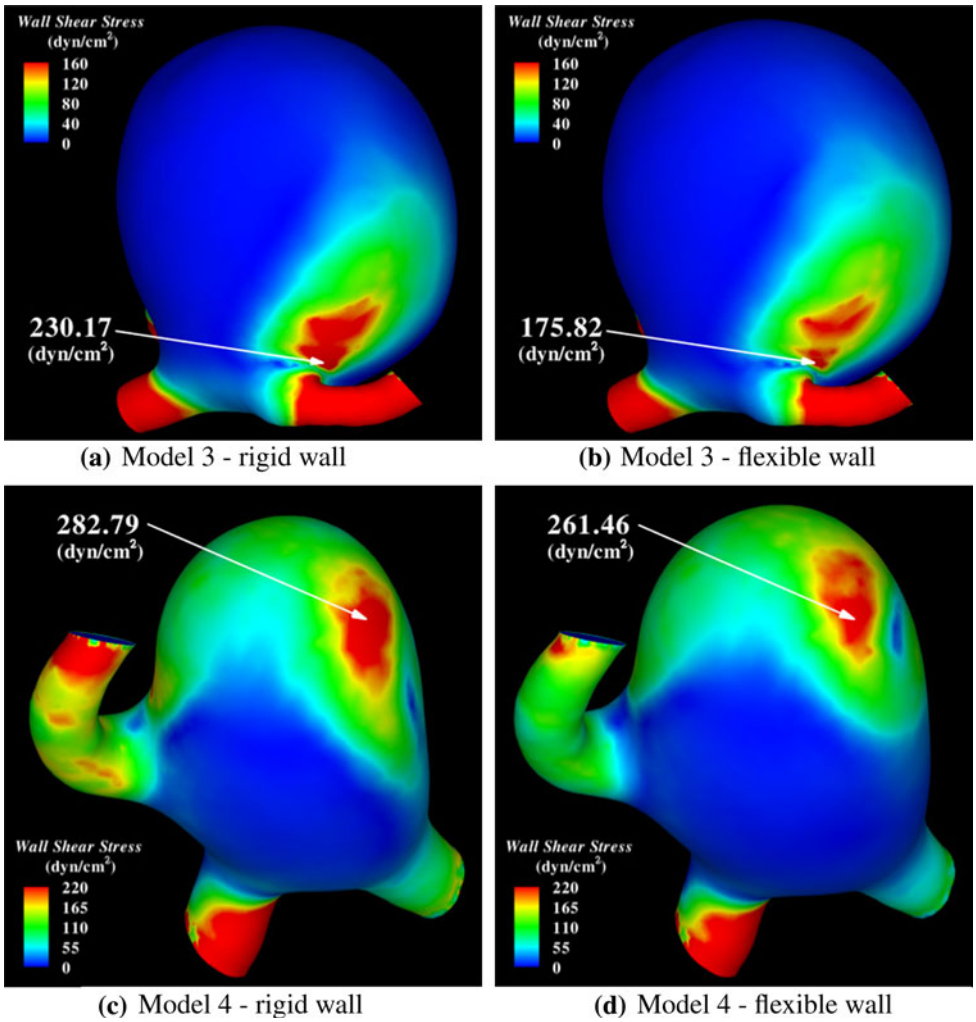

Fig. 10 Wall shear stress. Data taken near peak systole ($t = 0.08\,\mathrm{s}$)

are typically very thin and the largest stresses act in the in-plane directions. As a result, the natural quantity of interest is the principal in-plane stress, which we take for a definition of wall tension. We compute the WT as follows. Given the displacement field, we first compute the second Piola–Kirchhoff stress tensor from Eq. (1) and transform it to the Cauchy stress using Eq. (3). The Cauchy stress is then L_2-projected onto the space of the original tetrahedral finite element functions defined on the current configuration of the solid domain. As in the case of the fluid, this gives a convenient nodal definition of the Cauchy stress. The Cauchy stress, that is now defined on the outer boundary of the solid domain, is rotated to the local coordinate system on every boundary element face as

$$\boldsymbol{\sigma}^{s,l} = \boldsymbol{R}^T \boldsymbol{\sigma}^s \boldsymbol{R}. \tag{7}$$

The rotation matrix $\boldsymbol{R}$ takes the form

$$\boldsymbol{R} = \begin{bmatrix} \uparrow & \uparrow & \uparrow \\ \boldsymbol{t}_1^s & \boldsymbol{t}_2^s & \boldsymbol{n}^s \\ \downarrow & \downarrow & \downarrow \end{bmatrix}, \tag{8}$$

where $\boldsymbol{n}^s$ is the outward unit normal, and $\boldsymbol{t}_1^s$ and $\boldsymbol{t}_2^s$ are the two orthogonal tangent vectors on the outer surface of the solid.

Having rotated the stress tensor to the local coordinate system we modify it by directly imposing zero traction boundary conditions on the appropriate components of $\boldsymbol{\sigma}^{s,l}$, namely

$$\boldsymbol{\sigma}_{3i}^{s,l} = \boldsymbol{\sigma}_{i3}^{s,l} = 0 \quad \forall i = 1, 2, 3. \tag{9}$$

The eigenvalues of the resultant stress tensor can be computed by solving an appropriate quadratic equation. The wall tension is defined as the largest absolute eigenvalue, which also corresponds to the first principal in-pane stress.

Remark It should be noted that in the fully-continuous setting the zero normal stress boundary condition holds point-wise. This obviates the need to employ (9). However, in the discrete setting, the zero normal stress boundary condition only holds weakly. As a result, the exact point-wise satisfaction of this boundary condition is not guaranteed. The above procedure overwrites the computed values of the

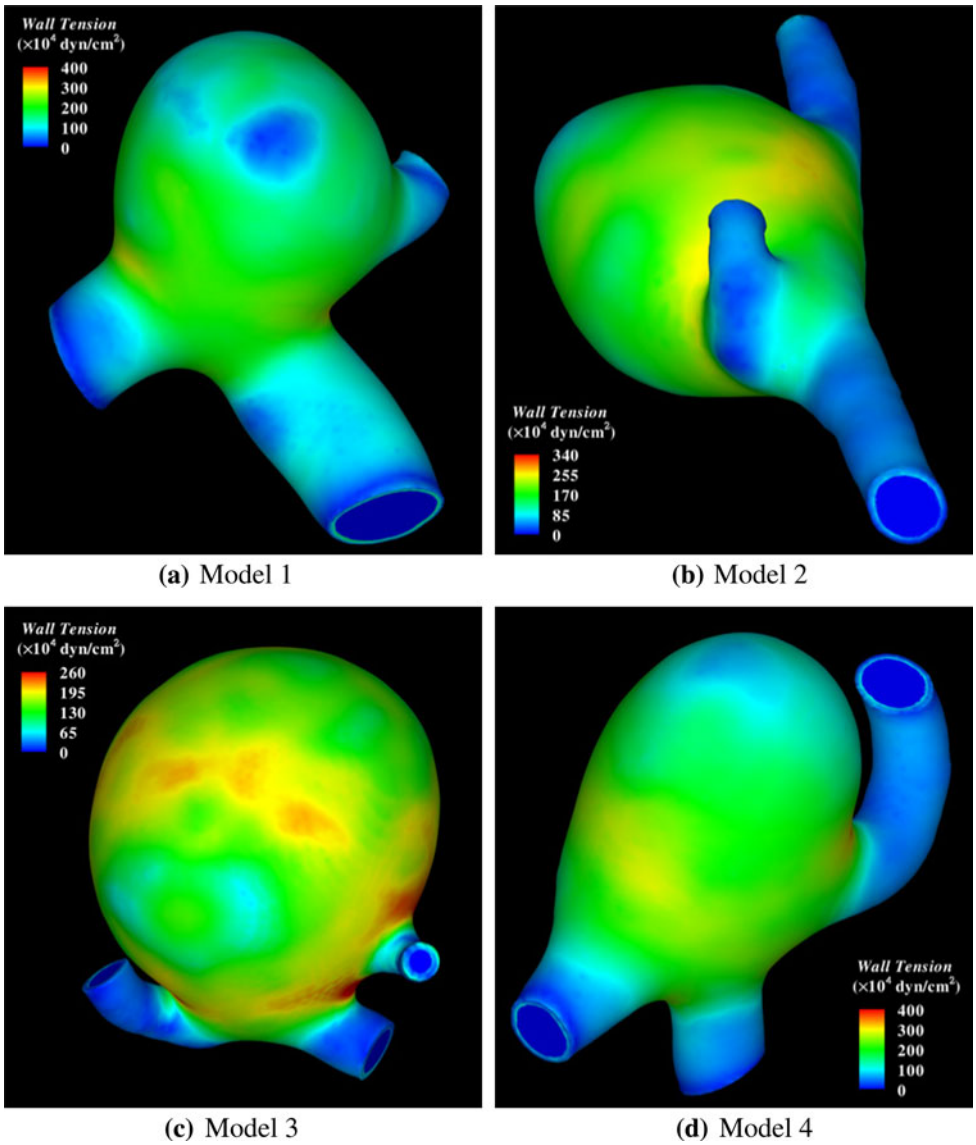

Fig. 11 Wall tension near low diastole ($t = 0.0$ s)

normal stress with their exact counterparts. This is often done in structural computations to enhance the accuracy of the computed stress fields (see, e.g., [18,30]).

4 Computational results

In this section, we present computational results for the four models we analyzed.

Figure 4 shows contours of the aneurysm wall displacement magnitude at peak systole, or highest inflow flowrate. The displacement is relative to a configuration at low diastole, or lowest flowrate. In Fig. 5 the models are superposed in the configurations corresponding to low diastole and peak systole for better visualization of the results. The relative displacement predicted is in good agreement with the observed movements during aneurysm surgery in the clinical practice of one of the authors, and predicted in computations by other researchers [36,43,44].

Figure 6 shows the blood flow velocity streamlines of Model 4 at various times during the heart cycle. The flow appears to be complex with several vortical features present, yet not turbulent. (By turbulence here we mean flow with a continuous cascade of temporal and spatial scales. See, for example, Pope [29].) Figures 7 and 8 show a comparison of blood flow speed at peak systole for the rigid and flexible wall simulations. Both rigid and flexible wall simulations predict similar flow speed distribution in the blood vessel. Among the cases considered, Model 4 shows the most difference. It should also be noted that Model 4 exhibits somewhat more complex flow features than the remaining models.

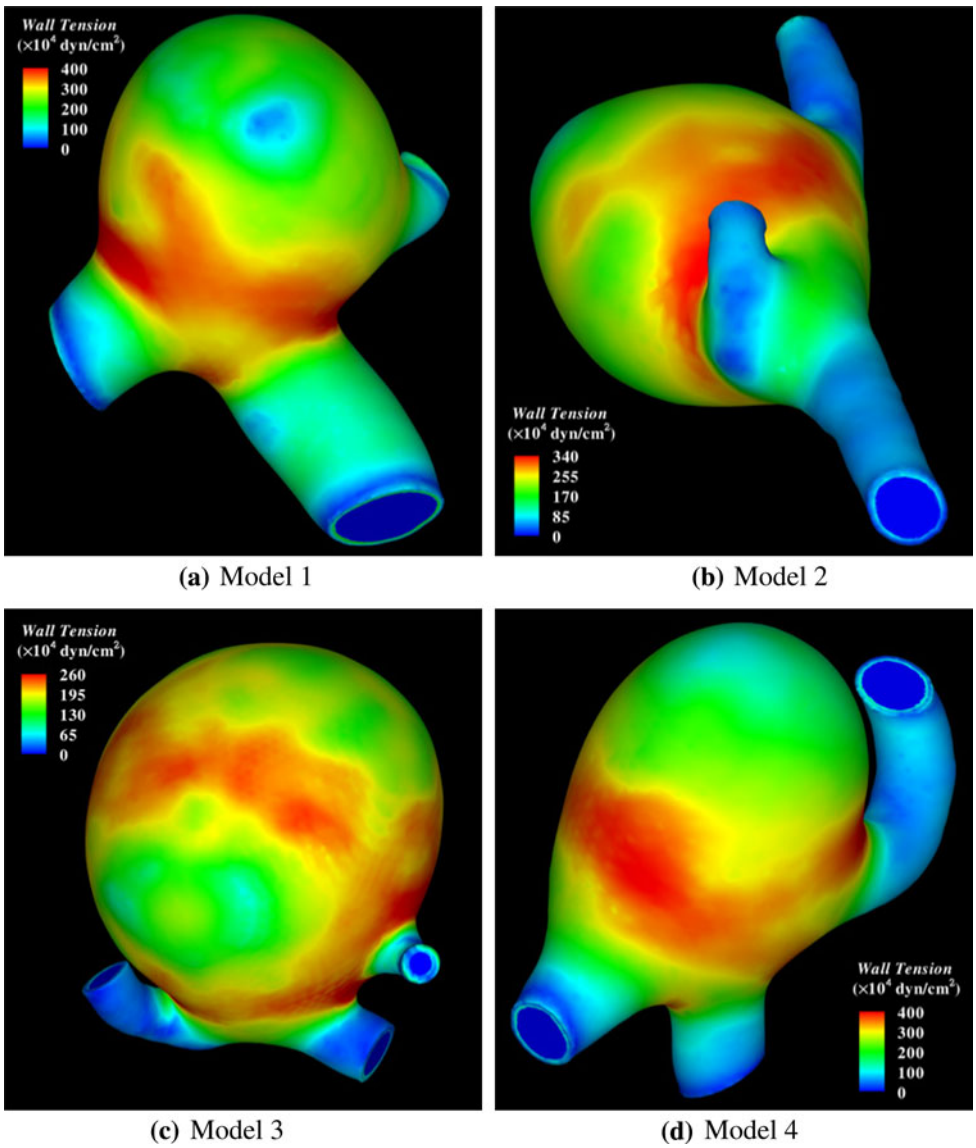

Fig. 12 Wall tension near peak systole ($t = 0.08$ s)

Figures 9 and 10 show the wall shear stress at the fluid-solid interface at the peak inflow flowrate. The wall shear stress in the aneurysm dome tends to reach its maximum near the region where the jet of blood coming from the inflow impinges on the aneurysm wall. Comparisons of the wall shear stress between the rigid and flexible wall cases are also shown in Figs. 9 and 10. In all cases the rigid wall assumption produces an over-estimate of the wall shear stress with respect to the flexible wall computations. Furthermore, the degree to which the wall shear stress is over-predicted is a strong function of the patient-specific geometry. In the case of Models 2 and 4, the percent error is relatively small (around 8%), while for Models 1 and 3 it is quite large (around 20% for Model 1 and 30% for Model 3). In the former cases, the jet of blood entering the aneurysm dome impinges on the wall in the direction normal to its surface. In the latter cases, the impingement occurs largely in the direction tangential to the wall surface. Also note that, in the cases of normal impingement, the resultant wall shear stress is significantly higher than in the cases of tangential impingement. We conclude that the relative orientation of the inflow branch and the aneurysm dome has a big influence on the wall shear stress distribution as well the importance of incorporating the effects of wall elasticity in the simulations. The authors feel that the difference of 30% in the wall shear stress prediction is significant and, given the importance of this hemodynamic quantity of interest, should not be overlooked in one's modeling choices.

The wall tension results are shown in Figs. 11 and 12. Figure 12 corresponds to the peak systole, while Fig. 11 corresponds to low diastole. The magnitude of the wall tension varies through the heart cycle due to the time-dependent nature of the flow. However, the relative wall tension

distribution does not vary significantly during the heart cycle. This is apparent from the figures. The wall tension also tends to concentrate near the areas of high aneurysm surface curvature. These observations suggest that the wall tension is largely driven by the intramural pressure and not so much by the viscous forces exerted on the arterial wall by the blood.

5 Conclusions

We presented a computational framework for the simulation of vascular FSI using patient-specific models. The methodology was applied to four patient-specific models of cerebral aneurysms to in part assess the relevance of including the elastic wall modeling in the simulations. The results show that the interaction between the blood flow and wall deformation significantly alters the hemodynamic forces acting on the arterial wall, with respect to the rigid wall case. The rigid wall simulations consistently overestimated the wall shear stress magnitude and, in one of the models, the gross features of the wall shear stress distribution on the arterial wall. Rigid versus flexible wall simulation results reinforce the importance of using FSI in the patient-specific modeling of cerebral aneurysms. Further observations show that the magnitude of the wall shear stress is a strong function of the inlet branch orientation and the angle of impingement of the blood on the arterial wall.

In the future, we plan to perform simulations of more patient-specific models so as to enhance our understanding of the underlying phenomena and their relationship to clinically observed events. We plan to increase the length of the inlet and outlet branches to minimize their effect on the computed solution, and also include a variable arterial wall thickness in the simulations. It is well known that the aneurysm wall is significantly thinner than that of the connecting branch vessels. The wall thickness is very hard or impossible to obtain experimentally, so we plan to make use of the geometry data (such as local branch radii, etc.) and clinical experience of one of the co-authors to incorporate a reasonable wall thickness of the aneurysm dome and the surrounding branch vessels in the simulations. Steps in this direction were already taken in [7], where a simple thickness reconstruction algorithm for blood vessels was proposed and employed in patient-specific simulations.

Acknowledgments We wish to thank the Texas Advanced Computing Center (TACC) at the University of Texas at Austin for providing HPC resources that have contributed to the research results reported within this paper. This work was partially supported by a research grant from the regional health authorities in northern Norway. Support of Teragrid Grant No. MCAD7S032 is also gratefully acknowledged. We thank Prof. Tor Ingebrigtsen, Institute for Clinical Medicine, University of Tromsø, Norway and the Department of Neurosurgery, the University Hospital of North Norway, for his clinical expertise to improve medical reality of the presented simulations.

References

1. Appanaboyina S, Mut F, Löhner R, Putman C, Cebral J (2009) Simulation of intracranial aneurysm stenting: techniques and challenges. Comput Methods Appl Mech Eng (published online) doi:10.1016/j.cma.2009.01.017
2. Badia S, Nobile F, Vergara C (2009) Robin-Robin preconditioned Krylov methods for fluid-structure interaction problems. Comput Methods Appl Mech Eng 198:2768–2784
3. Bazilevs Y, Calo VM, Cottrel JA, Hughes TJR, Reali A, Scovazzi G (2007) Variational multiscale residual-based turbulence modeling for large eddy simulation of incompressible flows. Comput Methods Appl Mech Eng 197:173–201
4. Bazilevs Y, Calo VM, Hughes TJR, Zhang Y (2008) Isogeometric fluid-structure interaction: theory, algorithms, and computations. Comput Mech 43:3–37
5. Bazilevs Y, Calo VM, Zhang Y, Hughes TJR (2006) Isogeometric fluid-structure interaction analysis with applications to arterial blood flow. Comput Mech 38:310–322
6. Bazilevs Y, Gohean JR, Hughes TJR, Moser RD, Zhang Y (2009) Patient-specific isogeometric fluid-structure interaction analysis of thoracic aortic blood flow due to implantation of the Jarvik 2000 left ventricular assist device. Comput Methods Appl Mech Eng (published online) doi:10.1016/j.cma.2009.04.015
7. Bazilevs Y, Hsu M-C, Benson DJ, Sankaran S, Marsden AL (2009) Computational fluid-structure interaction: methods and application to a total cavopulmonary connection. Comput Mech (in the same issue)
8. Bazilevs Y, Hughes TJR (2007) Weak imposition of Dirichlet boundary conditions in fluid mechanics. Comput Fluids 36:12–26
9. Brooks AN, Hughes TJR (1982) Streamline upwind/Petrov-Galerkin formulations for convection dominated flows with particular emphasis on the incompressible Navier–Stokes equations. Comput Methods Appl Mech Eng 32:199–259
10. Chung J, Hulbert GM (1993) A time integration algorithm for structural dynamics with improved numerical dissipation: the generalized-α method. J Appl Mech 60:371–375
11. Custus X. A visualization and navigation system for image-guided surgery based on VTK and ITK. http://www.sintef.no/Home/Health-Research/Medical-technology/
12. Fernández MA, Gerbeau J-F, Gloria A, Vidrascu M (2008) A partitioned Newton method for the interaction of a fluid and a 3D shell structure. Technical Report RR-6623, INRIA, 2008
13. Figueroa CA, Baek S, Taylor CA, Humphrey JD (2008) A computational framework for fluid-solid-growth modeling in cardiovascular simulations. Comput Methods Appl Mech Eng (published online) doi:10.1016/j.cma.2008.09.013
14. Figueroa CA, Vignon-Clementel IE, Jansen KE, Hughes TJR, Taylor CA (2006) A coupled momentum method for modeling blood flow in three-dimensional deformable arteries. Comput Methods Appl Mech Eng 195:5685–5706
15. Formaggia L, Gerbeau JF, Nobile F, Quarteroni A (2001) On the coupling of 3D and 1D Navier–Stokes equations for flow problems in compliant vessels. Comput Methods Appl Mech Eng 191:561–582
16. Gerbeau J-F, Vidrascu M, Frey P (2005) Fluid-structure interaction in blood flows on geometries based on medical imaging. Comput Struct 83:155–165

17. Holzapfel GA (2000) Nonlinear solid mechanics, a continuum approach for engineering. Wiley, Chichester
18. Hughes TJR, Cottrell JA, Bazilevs Y (2005) Isogeometric analysis: CAD, finite elements, NURBS, exact geometry, and mesh refinement. Comput Methods Appl Mech Eng 194:4135–4195
19. Hughes TJR, Engel G, Mazzei L, Larson MG (2000) The continuous Galerkin method is locally conservative. J Comput Phys 163:467–488
20. Hughes TJR, Oberai AA (2003) Calculation of shear stresses in the Fourier–Galerkin formulation of turbulent channel flows: projection, the Dirichlet filter and conservation. J Comput Phys 188: 281–295
21. Hughes TJR, Scovazzi G, Franca LP (2004) Multiscale and stabilized methods. In: Stein E, de Borst R, Hughes TJR (eds) Encyclopedia of Computational Mechanics, vol 3: Fluids, chapter 2. Wiley, London
22. Isaksen JG, Bazilevs Y, Kvamsdal T, Zhang Y, Kaspersen JH, Waterloo K, Romner B, Ingebrigtsen T (2008) Determination of wall tension in cerebral artery aneurysms by numerical simulation. Stroke 39:3172–3178
23. Jansen KE, Collis SS, Whiting C, Shakib F (1999) A better consistency for low-order stabilized finite element methods. Comput Methods Appl Mech Eng 174:153–170
24. Jansen KE, Whiting CH, Hulbert GM (1999) A generalized-α method for integrating the filtered Navier–Stokes equations with a stabilized finite element method. Comput Methods Appl Mech Eng 190:305–319
25. Lagana K, Dubini G, Migliavacca F, Pietrabissa R, Pennati G, Veneziani A, Quarteroni A (2002) Multiscale modelling as a tool to prescribe realistic boundary conditions for the study of surgical procedures. Biorheology 39:359–364
26. Lipton S, Evans JA, Bazilevs Y, Elguedj T, Hughes TJR (2009) Robustness of isogeometric structural discretizations under severe mesh distortion. Comput Methods Appl Mech Eng (published online) doi:10.1016/j.cma.2009.01.022
27. Marsden AL, Feinstein JA, Taylor CA (2008) A computational framework for derivative-free optimization of cardiovascular geometries. Comput Methods Appl Mech Eng 197:1890–1905
28. Oshima M, Hughes TJR, Jansen K (1998) Consistent finite element calculations of boundary and internal fluxes. Int J Comput Fluid Dyn 9:227–235
29. Pope SB (2001) Large-eddy simulation using projection onto local basis functions. In: Lumley JL (ed) Fluid mechanics and the environment: dynamical approaches, pp 239–265. Springer, Heidelberg
30. Rank E, Düster A, Nübel V, Preusch K, Bruhns OT (2005) High order finite elements for shells. Comput Methods Appl Mech Eng 194:2494–2512
31. Takizawa K, Christopher J, Moorman C, Martin J, Purdue J, McPhail T, Chen PR, Warren J, Tezduyar TE (2009) Space-time finite element computation of arterial FSI with patient-specific data. In: Schrefler B, Onate E, Papadrakakis M, (eds) Computational methods for coupled problems in science and engineering, coupled problems. CIMNE, Barcelona
32. Takizawa K, Christopher J, Tezduyar TE, Sathe S (2009) Space-time finite element computation of arterial fluid-structure interactions with patient-specific data. Commun Numer Methods Eng (published online) doi:10.1002/cnm.1241
33. Taylor CA, Hughes TJR, Zarins CK (1998) Finite element modeling of blood flow in arteries. Comput Methods Appl Mech Eng 158:155–196
34. Tezduyar TE (2003) Computation of moving boundaries and interfaces and stabilization parameters. Int J Numer Methods Fluids 43:555–575
35. Tezduyar TE, Sathe S (2007) Modelling of fluid-structure interactions with the space-time finite elements: solution techniques. Int J Numer Methods Fluids 54:855–900
36. Tezduyar TE, Sathe S, Cragin T, Nanna B, Conklin BS, Pausewang J, Schwaab M (2007) Modelling of fluid-structure interactions with the space-time finite elements: arterial fluid mechanics. Int J Numer Methods Fluids 54:901–922
37. Tezduyar TE, Sathe S, Schwaab M, Conklin BS (2008) Arterial fluid mechanics modeling with the stabilized space-time fluid-structure interaction technique. Int J Numer Methods Fluids 57:601–629
38. Tezduyar TE, Schwaab M, Sathe S (2008) Sequentially-coupled arterial fluid-structure interaction (SCAFSI) technique. Comput Methods Appl Mech Eng (published online) doi:10.1016/j.cma.2008.05.024
39. Tezduyar TE, Takizawa K (2008) Private communication
40. Torii R, Oshima M, Kobayashi T, Takagi K, Tezduyar TE (2006) Computer modeling of cardiovascular fluid-structure interactions with the deforming-spatial-domain/stabilized space-time formulation. Comput Methods Appl Mech Eng 195:1885–1895
41. Torii R, Oshima M, Kobayashi T, Takagi K, Tezduyar TE (2006) Fluid-structure interaction modeling of aneurysmal conditions with high and normal blood pressures. Comput Mech 38:482–490
42. Torii R, Oshima M, Kobayashi T, Takagi K, Tezduyar TE (2007) Influence of the wall elasticity in patient-specific hemodynamic simulations. Comput Fluids 36:160–168
43. Torii R, Oshima M, Kobayashi T, Takagi K, Tezduyar TE (2008) Fluid-structure interaction modeling of a patient-specific cerebral aneurysm: influence of structural modeling. Comput Mech 43:151–159
44. Torii R, Oshima M, Kobayashi T, Takagi K, Tezduyar TE (2008) Fluid-structure interaction modeling of blood flow and cerebral aneurysm: significance of artery and aneurysm shapes. Comput Methods Appl Mech Eng (published online) doi:10.1016/j.cma.2008.08.020
45. Vignon-Clementel IE, Figueroa CA, Jansen KE, Taylor CA (2006) Outflow boundary conditions for three-dimensional finite element modeling of blood flow and pressure in arteries. Comput Methods Appl Mech Eng 195:3776–3796
46. Zhang Y, Bajaj C, Sohn BS (2005) 3D finite element meshing from imaging data. Comput Methods Appl Mech Eng 194:5083–5106
47. Zhang Y, Wang W, Liang X, Bazilevs Y, Hsu M-C, Kvamsdal T, Brekken R, Isaksen JG (2009) High-fidelity tetrahedral mesh generation from medical imaging data for fluid-structure interaction analysis of cerebral aneurysms. Comput Model Eng Sci 42: 131–150
48. Zhang Y, Xu G, Bajaj C (2006) Quality meshing of implicit salvation models of biomolecular structures. Comput Aided Geom Des 23:510–530
49. Zunino P, D'Angelo C, Petrini L, Vergara C, Capelli C, Migliavacca F (2008) Numerical simulation of drug eluting coronary stents: Mechanics, fluid dynamics and drug release. Comput Methods Appl Mech Eng (published online) doi:10.1016/j.cma.2008.07.019